

RESEARCH

Open Access



Broadband beamforming of multiplet line arrays using subband optimal beamformers eliminating port/starboard ambiguity

Sergey Simakov*  and Simon Lourey

*Correspondence:

Sergey.Simakov@defence.gov.au

Sensors and Effectors Division,
Defence Science and Technology
Group, Edinburgh, SA 5111,
Australia

Abstract

Development of beamforming methods for towed sonar multiplet line arrays is stimulated by their increased use in undersea surveillance. Such methods employ various forms of narrowband optimal beamforming to resolve port/starboard ambiguity present when the array is conventionally beamformed. In this paper, we depart from the purely narrowband approach and discuss methods for port/starboard ambiguity rejection (PSAR) using a broadband formulation. The proposed methodology relies on subband beamforming for which we use non-adaptive variants of beamspace Minimum Variance Distortionless Response (MVDR) and the Linear Constraint Minimum Variance (LCMV) beamformers. We provide detailed description and comparison of both subband methods and establish a connection between them. The paper provides assessment of PSAR properties of the developed broadband beamformers using outputs of signal processing of both simulated and experimental sonar data. Experimental data for this work were obtained through the participation in the Littoral Continuous Active Sonar (LCAS) trials.

Keywords: Multiplet line arrays, Port/starboard ambiguity rejection, Optimal beamforming, Broadband processing

1 Introduction

Towed multiplet line arrays are increasingly used in undersea surveillance. A range of beamforming algorithms have been developed for such arrays, and most of them [1–5] focus on resolving the port/starboard ambiguity present when conventional towed line arrays are used, or when the towed line arrays are conventionally beamformed. The ambiguity is caused by the nearly conical shape of the resulting beampatterns. In this work, we are also concerned with beamforming algorithms developed for multiplet line arrays to efficiently resolve the port/starboard ambiguity. For completeness, we discuss both the narrowband and broadband cases.

The most straightforward approach to resolve the ambiguity is to employ null-steering in order to cancel the signal from the ambiguous direction [1, 4]. The resulting techniques use a form of the Linear Constraint Minimum Variance (LCMV) beamformer [6]. The LCMV method achieves the best port/starboard ambiguity rejection, but its

application is limited by the available degrees of freedom, which are reduced by each additional constraint. The total number of such degrees of freedom depends on the array configuration.

An alternative approach to deal with the port/starboard ambiguity is to employ the Minimum Variance Distortionless Response (MVDR) method. Adaptive forms of MVDR beamformers used in [2, 3] naturally treat the signal arriving from the ambiguous direction as an interference. All other interferences possibly present in the array input are also accounted for through estimation and application of the array covariance matrix. Unlike the LCMV method, the MVDR techniques are not limited by the available degrees of freedom.

Adaptive beamforming methods have been investigated extensively [6]. These methods require estimation of the array covariance matrix, which involves additional computational effort and imply a range of assumptions, including stationarity of the array input or invariability of the array shape during the listening interval. During their operation, the shapes of towed arrays and relative positions of receiver elements are continuously changing, which affects both the stationarity of the array input and the array manifold vectors used in the beamforming calculations.

In this work, we consider beamspace [7] non-adaptive variants of the MVDR [5] and LCMV beamformers. The discussed MVDR beamformer rejects the ambiguity by penalising the artificial interference arriving from the ambiguous direction. This is achieved by introducing the associated interference component into a synthetic beamspace array covariance matrix.

The noise component in the adopted approach is emulated using the isotropic noise model. The same noise model is used in the discussed LCMV method. In both methods, the beamforming coefficients are obtained using only the steering direction and a snapshot of the array shape at the considered time.

We also establish the connection between the considered MVDR and LCMV beamformers and derive conditions when the MVDR beamformer turns into the LCMV beamformer.

The beamspace approach reduces the computational effort and guarantees invertibility of the beamspace array covariance matrix.

The considered narrowband MVDR and LCMV beamformers are used to assemble the broadband beamformer. For completeness, we provide details of the broadband beamforming method employed in this work. The broadband beamforming method adopted in this work employs the subband approach [6]. Unlike the discrete Fourier transform beamformers [6], which treat each frequency bin as a subband, the considered beamformer operates on subbands made of many frequency bins, and, as a result, it requires significantly fewer beamforming operations.

The paper is organised as follows. Section 2 provides a continuous time formulation of the employed broadband beamforming approach, and specifics of the discrete-time implementation are provided in “Appendix”. Section 3 contains a detailed exposition of the narrowband beamforming methods used for beamforming subband components. In Sect. 4, we examine the port/starboard ambiguity rejection properties of the developed broadband beamformer using both the simulated sonar data and sonar data obtained through the participation in the Littoral Continuous Active Sonar (LCAS) trials.

2 Broadband beamforming using subband beamformers

Consider a receiver array made of Q elements. Let $\{\mathbf{d}_q\}$ ($q = 1, \dots, Q$) be the offsets of the receiver elements with respect to the array centre and c_{ss} be the average speed of sound at the location of the array. Pressure time series $p_q(t)$ obtained at different receiver elements form a real multi-channel signal $\mathbf{p}(t)$:

$$\mathbf{p}(t) = \begin{bmatrix} p_1(t) \\ \vdots \\ p_Q(t) \end{bmatrix}.$$

Let $\mathbf{P}(\omega)$ be the Fourier transform of $\mathbf{p}(t)$, that is,

$$\mathbf{P}(\omega) = \int e^{-i\omega t} \mathbf{p}(t) dt. \tag{1}$$

Since $\mathbf{p}(t)$ is real, we have $\mathbf{P}(-\omega) = \mathbf{P}^*(\omega)$. We assume that $\mathbf{p}(t)$ is band limited and so $\mathbf{P}(\omega)$ can be nonzero only when ω belongs to the intervals

$$-\omega_{\max} < \omega < -\omega_{\min} \quad \text{and} \quad \omega_{\min} < \omega < \omega_{\max} \tag{2}$$

where $\omega_{\max} > \omega_{\min} > 0$. Let $\{\hat{I}_s\}$ ($s = 1, \dots, N_s$) be a finite set of non-overlapping subbands covering the interval $(\omega_{\min}, \omega_{\max})$ and let $\{\omega_s\}$ be their centre frequencies. For each \hat{I}_s , define the associated rectangular window function

$$H_s^+(\omega) = \begin{cases} 1, & \omega \in \hat{I}_s \\ 0, & \text{otherwise} \end{cases}$$

Functions $H_s^+(\omega)$ form a partition of unity on the interval $(\omega_{\min}, \omega_{\max})$, i.e.

$$\sum_{s=1}^{N_s} H_s^+(\omega) = 1, \quad \omega \in (\omega_{\min}, \omega_{\max}).$$

Next define $H_s^-(\omega) = H_s^+(-\omega)$ and also introduce $H_s(\omega) = H_s^-(\omega) + H_s^+(\omega)$. Use the Fourier transform $\mathbf{P}(\omega)$ to represent $\mathbf{p}(t)$ as follows

$$\begin{aligned} \mathbf{p}(t) &= \frac{1}{2\pi} \int e^{i\omega t} \mathbf{P}(\omega) d\omega = \frac{1}{2\pi} \int e^{i\omega t} \sum_{s=1}^{N_s} H_s(\omega) \mathbf{P}(\omega) d\omega \\ &= \sum_{s=1}^{N_s} \frac{1}{2\pi} \int e^{i\omega t} H_s(\omega) \mathbf{P}(\omega) d\omega = \sum_{s=1}^{N_s} \mathbf{p}_s(t). \end{aligned} \tag{3}$$

Assuming that the bands \hat{I}_s are narrow, we can treat $\mathbf{p}_s(t)$ as a narrowband signal. Throughout this paper, notation $\mathcal{C}_\omega[g(t)]$ is used to denote a complex envelope [8, p. 73] of $g(t)$ obtained for the carrier frequency ω . Using ω_s as carrier frequencies for the respective narrowband components $\mathbf{p}_s(t)$, we obtain the complex envelopes

$$\tilde{\mathbf{p}}_s(t) = \mathcal{C}_{\omega_s}[\mathbf{p}_s(t)] \quad (s = 1, \dots, N_s). \tag{4}$$

Let \mathbf{v} be the unit vector of the steering direction. Introduce Q -by-1 vectors $\mathbf{x}_s(t)$ ($s = 1, \dots, N_s$) whose elements $[\mathbf{x}_s]_q$ are defined as follows

$$[\mathbf{x}_s]_q(t) = [\tilde{\mathbf{p}}_s]_q(t - \tau_q) \quad (q = 1, \dots, Q; s = 1, \dots, N_s), \tag{5}$$

where

$$\tau_q = \tau_q(\mathbf{v}) = (\mathbf{d}_q \cdot \mathbf{v})/c_{ss} \quad (q = 1, \dots, Q). \tag{6}$$

Application of the time delay τ_q aligns the equivalent baseband signals received at different receiver elements with that received at the centre of the array.

Each $\mathbf{x}_s(t)$ represents a complex narrowband array input in the frequency band \hat{I}_s . Next $\mathbf{x}_s(t)$ are beamformed using narrowband beamformers obtained for the carrier frequencies ω_s . The result of beamforming is scalar functions

$$y_s(t) = \mathbf{w}^H(\omega_s)\mathbf{x}_s(t) \quad (s = 1, \dots, N_s), \tag{7}$$

where $\mathbf{w}(\omega_s)$ are vectors of beamforming coefficients for frequency ω_s and the considered steering direction defined by the unit vector \mathbf{v} . (Here for brevity, the notation does not show the dependence of $\mathbf{w}(\omega_s)$ on \mathbf{v} .) We assume that the beamforming coefficients $\mathbf{w}(\omega_s)$ satisfy the distortionless response conditions

$$\mathbf{w}^H(\omega_s)\mathbf{v}_s(\omega_s, \mathbf{v}) = 1, \tag{8}$$

where $\mathbf{v}_s(\omega_s, \mathbf{v})$ is the array manifold vector [6]

$$\mathbf{v}_s(\omega_s, \mathbf{v}) = \begin{bmatrix} e^{i\omega_s\tau_1} \\ \vdots \\ e^{i\omega_s\tau_Q} \end{bmatrix}. \tag{9}$$

To combine $y_s(t)$ into a single output, we need to transform the complex envelopes obtained for different carrier frequencies ω_s into complex envelopes corresponding to a single carrier frequency ω_0

$$y_s(t) \mapsto y_s(t)e^{i(\omega_s-\omega_0)t} \quad (s = 1, \dots, N_s).$$

The resulting broadband beamformer output is

$$y(t) = \sum_{s=1}^{N_s} \mathbf{w}^H(\omega_s)\mathbf{x}_s(t)e^{i(\omega_s-\omega_0)t}. \tag{10}$$

Suppose the array receives only a signal arriving from the steering direction \mathbf{v} . If $g(t)$ is the associated dynamic pressure at the centre of the array and $G(\omega)$ is its Fourier transform, then

$$[\mathbf{p}_s]_q(t) = g_s(t + \tau_q),$$

where

$$g_s(t) = \frac{1}{2\pi} \int e^{i\omega t} H_s(\omega) G(\omega) d\omega.$$

Use (5) to obtain

$$[\mathbf{x}_s]_q(t) = [\tilde{\mathbf{p}}_s]_q(t - \tau_q) = \tilde{g}_s(t) e^{i\omega_s \tau_q}, \tag{11}$$

where $\tilde{g}_s(t) = \mathcal{C}_{\omega_s}[g_s(t)]$. Use (9) to rewrite (11) as

$$\mathbf{x}_s(t) = \tilde{g}_s(t) \mathbf{v}_s. \tag{12}$$

Substitution of (12) into (10) and application of the distortionless response condition (8) give

$$y(t) = \sum_{s=1}^{N_s} \mathbf{w}^H(\omega_s) \mathbf{v}_s \tilde{g}_s(t) e^{i(\omega_s - \omega_0)t} = \sum_{s=1}^{N_s} \mathcal{C}_{\omega_0}[g_s(t)] = \mathcal{C}_{\omega_0}[g(t)]. \tag{13}$$

Equation (13) shows that the considered broadband beamformer (10) transforms the signal component of the array input into the beamforming output without distortion. The distortionless response property of the beamformer streamlines further signal processing. In particular, it simplifies the selection of a replica used in matched filtering.

Specifics of a discrete-time implementation of the scheme described in this section are provided in “Appendix”.

3 Subband beamformers for multiplet line arrays

The broadband beamforming method described in Sect. 2 requires subband beamforming coefficient vectors $\mathbf{w}(\omega_s)$. In this section, we discuss two techniques for subband beamforming of multiplet line arrays. In these techniques, $\mathbf{w}(\omega)$ is built so as to eliminate the port/starboard ambiguity typically present when line arrays are conventionally beamformed. Both techniques employ the beamspace approach, and they rely on the use of synthetic clutter covariance matrices and treat the arrival from the ambiguous direction as an interference. The first of these techniques is based on the MVDR [6, p. 452] method, while the other employs the LCMV [6, p. 513] method.

3.1 Multiplet line arrays and beamspace beamforming

Consider a towed sonar array made of K multiplets, each consisting of L receiver elements. A receiver element can be identified by the numbers k and ℓ , the sequential number of its multiplet and the sequential number of the element within the multiplet, respectively (see Fig. 1). Alternatively, receiver element (k, ℓ) can be identified using a single linear index $q = \eta(k, \ell)$, where

$$\eta(k, \ell) = \ell + L(k - 1). \tag{14}$$

If ℓ is fixed, a combination of array elements $q = \eta(k, \ell)$ for $k = 1, \dots, K$ forms a linear subarray.

Suppose that multi-channel pressure time series $\mathbf{p}_{\text{nb}}(t)$ received by the array has a spectrum confined to a narrow band centred at frequency ω . If $\omega = \omega_s$, then the results derived for $\mathbf{p}_{\text{nb}}(t)$ will be readily applicable to the subband components $\mathbf{p}_s(t)$ defined in Eq. (3). Let $\tilde{\mathbf{p}}_{\text{nb}}(t)$ be the complex envelope of $\mathbf{p}_{\text{nb}}(t)$ obtained for the carrier frequency ω . Similarly to (5) define the *aligned* multi-channel array signal $\mathbf{x}(t)$ as

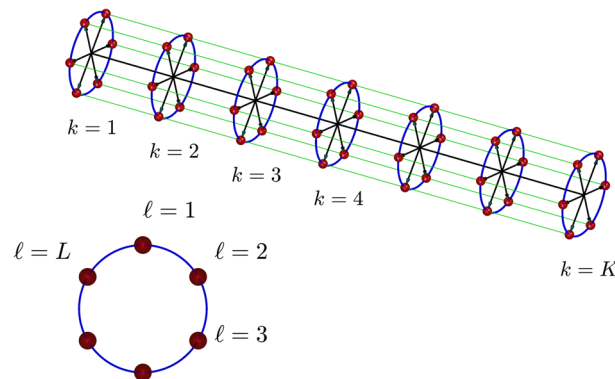


Fig. 1 Schematic diagram illustrating the geometry of a multiplet line array

$$x_q(t) = [\mathbf{x}(t)]_q = [\tilde{\mathbf{p}}_{\text{nb}}]_q(t - \tau_q), \tag{15}$$

where $q = 1, \dots, Q$, and the delays τ_q are defined by Eq. (6).

Our aim is to build a beamforming vector $\mathbf{w} = \mathbf{w}(\omega)$ required to produce the subband beamformed signal

$$y_{\text{nb}}(t) = \mathbf{w}^H \mathbf{x}(t). \tag{16}$$

To achieve this we adopt a beamspace approach [2, 5, 7] in which $y_{\text{nb}}(t)$ is obtained as a linear combination of outputs $z_\ell(t)$ of conventionally beamformed linear subarrays ℓ , that is,

$$y_{\text{nb}}(t) = h_1^* z_1(t) + \dots + h_L^* z_L(t) = [h_1^*, \dots, h_L^*] \begin{bmatrix} z_1(t) \\ \vdots \\ z_L(t) \end{bmatrix} = \mathbf{h}^H \mathbf{z}. \tag{17}$$

To express $z_\ell(t)$ in terms of $x_q(t)$, for each subarray ℓ , define the associated multi-channel signal

$$\mathbf{x}^{[\ell]}(t) = \begin{bmatrix} x_{1,\ell}(t) \\ \vdots \\ x_{K,\ell}(t) \end{bmatrix}, \tag{18}$$

where $x_{k,\ell}(t) = x_{\eta(k,\ell)}(t)$. Also, for each subarray ℓ , define the array manifold vector \mathbf{v}_ℓ

$$\mathbf{v}_\ell = \mathbf{v}_\ell(\boldsymbol{\nu}) = \begin{bmatrix} v_{1,\ell}(\boldsymbol{\nu}) \\ \vdots \\ v_{K,\ell}(\boldsymbol{\nu}) \end{bmatrix} = \begin{bmatrix} e^{i\omega\tau_{1,\ell}} \\ \vdots \\ e^{i\omega\tau_{K,\ell}} \end{bmatrix}, \tag{19}$$

where $\tau_{k,\ell} = \tau_{\eta(k,\ell)}$ and τ_q are defined by (6). Use (18) and (19) to obtain

$$z_\ell(t) = \mathbf{v}_\ell^H(\boldsymbol{\nu}) \mathbf{x}^{[\ell]}(t). \tag{20}$$

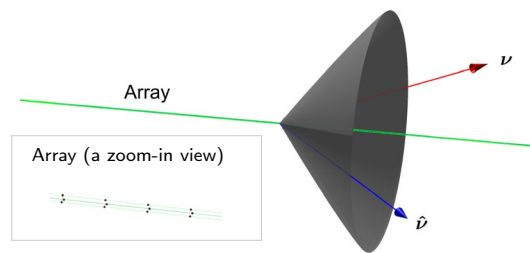


Fig. 2 The beam pattern of a conventionally beamformed towed multiplet line array has a nearly conic shape

Equation (20) allows us to revert from (17) to (16) by expressing \mathbf{w} in terms of \mathbf{h}

$$w_{\eta(k,\ell)} = h_{\ell} e^{i\omega\tau_{k,\ell}}. \tag{21}$$

The beamspace beamforming consists in building the beamspace beamforming vector \mathbf{h} . For example, setting $h_{\ell} = 1$ for $\ell = 1, \dots, L$, results in a conventional beamformer. The beam pattern of a conventionally beamformed towed multiplet line array has a nearly conic shape (see Fig. 2). As a consequence, beamforming results obtained for a steering direction \mathbf{v} happen to be the same as those obtained for the axially symmetric direction $\hat{\mathbf{v}}$. This effect is known as the *port/starboard* (or *left/right ambiguity*). Removal of such ambiguity can be carried out by appropriately shaping the array’s beam pattern. One way to achieve this is by using the MVDR beamforming applied to a synthetic clutter consisting of an isotropic noise and an interference arriving from the ambiguous direction $\hat{\mathbf{v}}$. The details of the method are summarised below.

3.2 Subband beamforming using the beamspace MVDR method

We employ an optimal beamforming technique [6] that maximises the gain

$$G(\mathbf{h}) = \frac{\mathcal{E}_a(\mathbf{h})/P_{a:ni}(\mathbf{h})}{\mathcal{E}_{el}/P_{el:ni}}, \tag{22}$$

where

- \mathcal{E}_{el} is the energy of the echo received by a single receiver element,
- $P_{el:ni}$ is the power of the combined noise and interference process received by a single receiver element,
- $\mathcal{E}_a(\mathbf{h})$ is the energy of the echo-only component of the beamformed array output,
- $P_{a:ni}(\mathbf{h})$ is the combined noise and interference array output power.

Suppose that the narrowband echo arrives from the steering direction \mathbf{v} . If the dynamic pressure induced by the echo at the centre of the array is $g(t)$ and its complex envelope is $\tilde{g}(t) = \mathcal{C}_{\omega}[g(t)]$, then

$$\mathcal{E}_{el} = \frac{1}{2} \int |\tilde{g}(t)|^2 dt. \tag{23}$$

To obtain \mathcal{E}_a , we first note that the echo-only aligned multi-channel signal for subarray ℓ is

$$\mathbf{x}^{[\ell]}(t) = \tilde{g}(t)\mathbf{v}_\ell(\mathbf{v}).$$

By (17) and (20), the resulting beamformed array output is

$$y_{\text{nb}}^{\text{echo}}(t) = \tilde{g}(t)\mathbf{h}^H \begin{bmatrix} \mathbf{v}_1^H(\mathbf{v})\mathbf{v}_1(\mathbf{v}) \\ \vdots \\ \mathbf{v}_L^H(\mathbf{v})\mathbf{v}_L(\mathbf{v}) \end{bmatrix} = K \tilde{g}(t)\mathbf{h}^H \mathbf{u}(\mathbf{v}, \mathbf{v}) = K \tilde{g}(t)\mathbf{h}^H \mathbf{u}_0, \tag{24}$$

where

$$\mathbf{u}(\mathbf{v}_a, \mathbf{v}_b) = \frac{1}{K} \begin{bmatrix} \mathbf{v}_1^H(\mathbf{v}_a)\mathbf{v}_1(\mathbf{v}_b) \\ \vdots \\ \mathbf{v}_L^H(\mathbf{v}_a)\mathbf{v}_L(\mathbf{v}_b) \end{bmatrix} \tag{25}$$

and

$$\mathbf{u}_0 = \begin{bmatrix} 1 \\ \vdots \\ 1 \end{bmatrix}. \tag{26}$$

Use (24) to obtain

$$\mathcal{E}_a(\mathbf{h}) = \frac{1}{2} \int |y_{\text{nb}}^{\text{echo}}(t)|^2 dt = \frac{K^2}{2} |\mathbf{h}^H \mathbf{u}_0|^2 \int |\tilde{g}(t)|^2 dt. \tag{27}$$

The synthetic clutter employed in our method consists of an isotropic noise and an interference arriving from the direction $\hat{\mathbf{v}}$. These two processes are assumed to be independent. We also assume that the narrowband acoustic process $g_i(t)$ induced by the interference arriving at the centre of the array from direction $\hat{\mathbf{v}}$ is stationary and $E[|g_i(t)|^2] = \sigma_i^2$. Suppose the bandwidth of this process is small enough that variations of $\tilde{g}_i(t) \equiv C_\omega[g_i(t)]$ within time intervals of length $\max_k(|\mathbf{d}_k|)/c_{\text{ss}}$ can be ignored. Then, the interference component of the pre-beamformed signal for subarray ℓ is $\mathbf{x}^{[\ell]}(t) = \tilde{g}_i(t)\mathbf{v}_\ell(\hat{\mathbf{v}})$, and the associated beamspace covariance matrix is

$$\mathbf{R}_{z:i} \equiv E[\mathbf{z}\mathbf{z}^H] = 2\sigma_i^2 K^2 \hat{\mathbf{u}}\hat{\mathbf{u}}^H, \tag{28}$$

where

$$\hat{\mathbf{u}} = \mathbf{u}(\mathbf{v}, \hat{\mathbf{v}}). \tag{29}$$

The noise component of the proposed synthetic clutter is similarly assumed to be a stationary narrowband process. Let the variance of the associated dynamic pressure be σ_n^2 . The noise beamspace array covariance matrix is

$$\mathbf{R}_{\mathbf{z};n} = E \left[\begin{bmatrix} \zeta_1(t) \\ \vdots \\ \zeta_L(t) \end{bmatrix} \begin{bmatrix} \zeta_1^*(t) & \cdots & \zeta_L^*(t) \end{bmatrix} \right], \tag{30}$$

where

$$\zeta_\ell(t) = \mathbf{v}_\ell^H(\mathbf{v}) \mathbf{n}_\ell(t), \quad \text{and} \quad \mathbf{n}_\ell(t) = \begin{bmatrix} n_{1,\ell}(t) \\ \vdots \\ n_{K,\ell}(t) \end{bmatrix},$$

while $n_{k,\ell}(t)$ is the complex envelope of the noise process at receiver element $q = \eta(k, \ell)$. The elements of $\mathbf{R}_{\mathbf{z};n}$ are obtained using

$$[\mathbf{R}_{\mathbf{z};n}]_{\ell p} = \mathbf{v}_\ell^H(\mathbf{v}) E \left[\mathbf{n}_\ell(t) \mathbf{n}_p^H(t) \right] \mathbf{v}_p(\mathbf{v}) = \sum_{k=1}^K \sum_{s=1}^K v_{k,\ell}^*(\mathbf{v}) v_{s,p}(\mathbf{v}) E \left[n_{k,\ell} n_{s,p}^* \right]. \tag{31}$$

Since the noise is assumed to be isotropic, we have [9]

$$E \left[n_{k,\ell} n_{s,p}^* \right] = 2\sigma_n^2 \text{sinc}(\omega |\mathbf{d}_{\eta(k,\ell)} - \mathbf{d}_{\eta(s,p)}| / c_{ss}). \tag{32}$$

Note that the proposed synthetic noise covariance could also include a component associated with the independent noise. In this case, $E \left[n_{k,\ell} n_{s,p}^* \right]$ takes the form

$$E \left[n_{k,\ell} n_{s,p}^* \right] = \frac{2\sigma_n^2}{1 + \varkappa} \left[\text{sinc} \left(\frac{\omega |\mathbf{d}_{\eta(k,\ell)} - \mathbf{d}_{\eta(s,p)}|}{c_{ss}} \right) + \varkappa \delta_{\eta(k,\ell), \eta(s,p)} \right], \tag{33}$$

where δ_{η_1, η_2} is the Kronecker delta and \varkappa controls the proportion of the independent component included in the noise covariance.

The combined noise and interference array output power is

$$P_{\text{a;ni}}(\mathbf{h}) = \frac{1}{2} \mathbf{h}^H \mathbf{R}_{\mathbf{z};ni} \mathbf{h}. \tag{34}$$

where $\mathbf{R}_{\mathbf{z};ni}$ is the associated array covariance matrix. The proposed noise and interference are independent, so $\mathbf{R}_{\mathbf{z};ni} = \mathbf{R}_{\mathbf{z};n} + \mathbf{R}_{\mathbf{z};i}$.

The power of the combined noise and interference process at a single receiver element is

$$P_{\text{el;ni}} = \sigma_n^2 + \sigma_i^2. \tag{35}$$

Substitution of (23), (27), (34) and (35) into (22) gives

$$G(\mathbf{h}) = 2K^2 (\sigma_n^2 + \sigma_i^2) \frac{|\mathbf{h}^H \mathbf{u}_0|^2}{\mathbf{h}^H \mathbf{R}_{\mathbf{z};ni} \mathbf{h}}. \tag{36}$$

It follows from the Cauchy–Schwarz inequality that $G(\mathbf{h})$ achieves its maximum at

$$\mathbf{h} = \frac{1}{K} \frac{\mathbf{R}_{\mathbf{z};ni}^{-1} \mathbf{u}_0}{\mathbf{u}_0^H \mathbf{R}_{\mathbf{z};ni}^{-1} \mathbf{u}_0}. \tag{37}$$

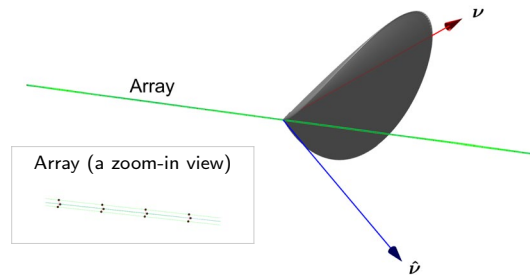


Fig. 3 The beampattern of the designed optimal beamspace beamformer is suppressed in the ambiguous direction

An example of the resulting beampattern obtained for the same steering direction as in Fig. 2 is provided in Fig. 3. The optimal beamformer suppresses the artificial interference arriving from the ambiguous direction $\hat{\mathbf{v}}$ and eliminates the port/starboard ambiguity.

Solution (37) satisfies

$$\mathbf{h}^H \mathbf{u}_0 = \sum_{\ell=1}^L h_{\ell}^* = 1/K. \tag{38}$$

Equations (21) and (38) give

$$\mathbf{w}^H \mathbf{v}(\mathbf{v}) = \sum_{\ell=1}^L \sum_{k=1}^K h_{\ell}^* e^{-i\omega\tau_{k,\ell}(\mathbf{v})} e^{i\omega\tau_{k,\ell}(\mathbf{v})} = K \sum_{\ell=1}^L h_{\ell}^* = 1, \tag{39}$$

which confirms that the beamformer defined by (17) and (37) satisfies the distortionless response requirement (8).

The result (37) can also be obtained by considering the following constrained optimisation problem

Minimise the output clutter power (34) subject to the distortionless response constraint (38). (40)

Minimisation of (34) is equivalent to minimisation of the variance of the clutter component for a given clutter covariance matrix. Following [6, p. 452], we refer to the formulation (40) and the result (37) using the Minimum Variance Distortionless Response (MVDR) descriptor. An adaptive form of (40) would minimise $\mathbf{h}^H \mathbf{R}_z \mathbf{h}$ instead of $\mathbf{h}^H \mathbf{R}_{z:\text{ni}} \mathbf{h}$, where $\mathbf{R}_z = E[\mathbf{z}\mathbf{z}^H]$ is estimated using the received sonar data. This approach was employed in [2] and [3]. Following [6, p. 451], we refer to the associated method using the Minimum Power Distortionless Response (MPDR) descriptor. Note that the terms MVDR and MPDR are often used interchangeably [6, p. 451].

The workflow for computation of the MVDR subband beamforming coefficients is illustrated in Fig. 4. Given the frequency ω , the steering direction vector \mathbf{v} and the receiver element locations $\{\mathbf{d}_q\}$, we first use (19) and (28)–(32) to obtain the associated $\{\mathbf{v}_{\ell}(\omega, \mathbf{v})\}$ and $\mathbf{R}_{z:\text{ni}}(\omega, \mathbf{v})$. Next we use (37) to compute the beamspace beamforming vector $\mathbf{h}(\omega, \mathbf{v})$. The subband beamforming vector $\mathbf{w}(\omega, \mathbf{v})$ is obtained from $\mathbf{h}(\omega, \mathbf{v})$ and $\{\mathbf{v}_{\ell}(\omega, \mathbf{v})\}$ using (21).

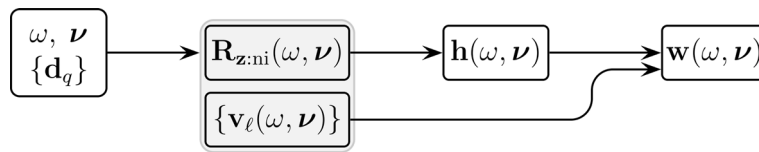


Fig. 4 Workflow for computation of MVDR subband beamforming coefficients

3.3 Subband beamforming using the beamspace LCMV method

When the echo arrives from the ambiguous direction $\hat{\mathbf{v}}$, then the beamformer output associated with the echo is

$$y_{\text{nb}}^{\text{echo}}(t, \mathbf{v}, \hat{\mathbf{v}}) = K \tilde{g}(t) \mathbf{h}^H \hat{\mathbf{u}}, \tag{41}$$

where $\hat{\mathbf{u}}$ is given by (29). In order to eliminate the resulting ambiguity, we suppress this output, following [4], by imposing the null-steering constraint

$$\mathbf{h}^H \hat{\mathbf{u}} = 0. \tag{42}$$

As before we assume that the synthetic ambient noise is isotropic so the associated covariance matrix $\mathbf{R}_{z:n}$ is obtained using (30)–(32).

Setting the objective to optimise the noise power subject to the distortionless response and null-steering constraints, we arrive at the following *Linear Constrained Minimum Variance* (LCMV) [6, p. 513–514] formulation.

$$\text{Minimise the output noise power } P_{\text{a:n}} = \frac{1}{2} \mathbf{h}^H \mathbf{R}_{z:n} \mathbf{h} \text{ subject to the constraints (38) and (42).} \tag{43}$$

Defining

$$\mathbf{C} = K[\mathbf{u}_0 \hat{\mathbf{u}}] \quad \text{and} \quad \mathbf{g} = \begin{bmatrix} 1 \\ 0 \end{bmatrix}, \tag{44}$$

we obtain that the solution of (43) has the following form [6, p. 527]

$$\mathbf{h} = \mathbf{R}_{z:n}^{-1} \mathbf{C} \left[\mathbf{C}^H \mathbf{R}_{z:n}^{-1} \mathbf{C} \right]^{-1} \mathbf{g}. \tag{45}$$

The workflow for computation of the LCMV subband beamforming coefficients is illustrated in Fig. 5. Given the frequency ω , the steering direction vector \mathbf{v} and the receiver element locations $\{\mathbf{d}_q\}$, we first use (19), (30)–(32) and (44) to obtain the associated $\{\mathbf{v}_\ell(\omega, \mathbf{v})\}$, $\mathbf{R}_{z:n}(\omega, \mathbf{v})$ and $\mathbf{C}(\omega, \mathbf{v})$. Next we use (45) to compute the beamspace beamforming vector $\mathbf{h}(\omega, \mathbf{v})$. The subband beamforming vector $\mathbf{w}(\omega, \mathbf{v})$ is obtained from $\mathbf{h}(\omega, \mathbf{v})$ and $\{\mathbf{v}_\ell(\omega, \mathbf{v})\}$ using (21).

Unlike their adaptive MPDR and LCMP counterparts, the non-adaptive variants of MVDR and LCMV discussed above do not rely on the use of the sonar data. Both the workflows (4) and (5) for computation of the subband beamforming coefficients require the receiver element positions, the subband frequency and the steering direction. The resulting beampatterns are obtained using synthetic constructs which emulate the actual acoustic configuration.

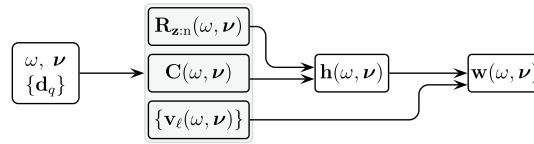


Fig. 5 Workflow for computation of LCMV subband beamforming coefficients

3.4 Comparison of the MVDR and LCMV beamforming coefficients

The MVDR and LCMV beamforming coefficient vectors \mathbf{h}_{MVDR} and \mathbf{h}_{LCMV} are obtained using Eqs. (37) and (45), respectively. To establish connection between \mathbf{h}_{MVDR} and \mathbf{h}_{LCMV} , we first note that the result (45) is equivalent to

$$\mathbf{h}_{\text{LCMV}} = \frac{1}{K} \frac{\mathbf{R}_{z:n}^{-1} \mathbf{u}_0 \hat{\mathbf{u}}^H \mathbf{R}_{z:n}^{-1} \hat{\mathbf{u}} - \mathbf{R}_{z:n}^{-1} \hat{\mathbf{u}} \hat{\mathbf{u}}^H \mathbf{R}_{z:n}^{-1} \mathbf{u}_0}{\mathbf{u}_0^H \mathbf{R}_{z:n}^{-1} \mathbf{u}_0 \hat{\mathbf{u}}^H \mathbf{R}_{z:n}^{-1} \hat{\mathbf{u}} - \mathbf{u}_0^H \mathbf{R}_{z:n}^{-1} \hat{\mathbf{u}} \hat{\mathbf{u}}^H \mathbf{R}_{z:n}^{-1} \mathbf{u}_0}. \tag{46}$$

Equation (46) can be readily obtained using substitution of (44) into (45) followed by routine algebraic steps. Next we use Woodbury’s identity (e.g. see [6, p. 1348]) to obtain

$$\mathbf{R}_{z:ni}^{-1} \mathbf{u}_0 = \mathbf{R}_{z:n}^{-1} \mathbf{u}_0 - \frac{2\sigma_i^2 K^2 \mathbf{R}_{z:n}^{-1} \hat{\mathbf{u}} \hat{\mathbf{u}}^H \mathbf{R}_{z:n}^{-1} \mathbf{u}_0}{1 + 2\sigma_i^2 K^2 \hat{\mathbf{u}}^H \mathbf{R}_{z:n}^{-1} \hat{\mathbf{u}}}. \tag{47}$$

If $\sigma_i^2 \gg \sigma_n^2$, then $2\sigma_i^2 K^2 \hat{\mathbf{u}}^H \mathbf{R}_{z:n}^{-1} \hat{\mathbf{u}} \gg 1$, so Eq. (47) can be written as

$$\mathbf{R}_{z:ni}^{-1} \mathbf{u}_0 = \frac{\mathbf{R}_{z:n}^{-1} \mathbf{u}_0 \hat{\mathbf{u}}^H \mathbf{R}_{z:n}^{-1} \hat{\mathbf{u}} - \mathbf{R}_{z:n}^{-1} \hat{\mathbf{u}} \hat{\mathbf{u}}^H \mathbf{R}_{z:n}^{-1} \mathbf{u}_0}{\hat{\mathbf{u}}^H \mathbf{R}_{z:n}^{-1} \hat{\mathbf{u}}}. \tag{48}$$

Substitution of (48) into Eq. (37) gives the same expression as in the right-hand part of (46). Hence, the MVDR beamforming vector \mathbf{h}_{MVDR} turns into the LCMV beamforming vector \mathbf{h}_{LCMV} when $\sigma_i^2 \gg \sigma_n^2$. This result can also be demonstrated by showing that the MVDR beamformer places a perfect null on the interfering signal when $\sigma_i^2/\sigma_n^2 \rightarrow \infty$ (e.g. see [6, p. 455]).

3.5 Dealing with interferences with known directions of arrival

The discussed beamspace methods suppress the beampattern in the ambiguous direction by considering an emulated acoustic field and treating the echo arriving from that direction as an interference. Suppose now that the actual acoustic signal received by the array also contains J interferences arriving from known directions \mathbf{v}_j ($j = 1, \dots, J$). To suppress the beampattern in the directions \mathbf{v}_j using the MVDR method, we modify the emulated array covariance $\mathbf{R}_{z:ni}$ as follows

$$\mathbf{R}_{z:ni} = \mathbf{R}_{z:n} + 2\sigma_i^2 K^2 \hat{\mathbf{u}} \hat{\mathbf{u}}^H + 2 \sum_{j=1}^J \sigma_j^2 K^2 \mathbf{u}_j \mathbf{u}_j^H. \tag{49}$$

where $\mathbf{u}_j = \mathbf{u}(\mathbf{v}_j)$. The additional terms in (49) are derived in the same way as (28). The associated beamforming vector \mathbf{h}_{MVDR} is obtained by substituting (49) into (37).

In the LCMV case, in order to suppress the beampattern in direction \mathbf{v}_j , we modify the linear constraint matrices by adding a column \mathbf{u}_j to matrix \mathbf{C} and a corresponding

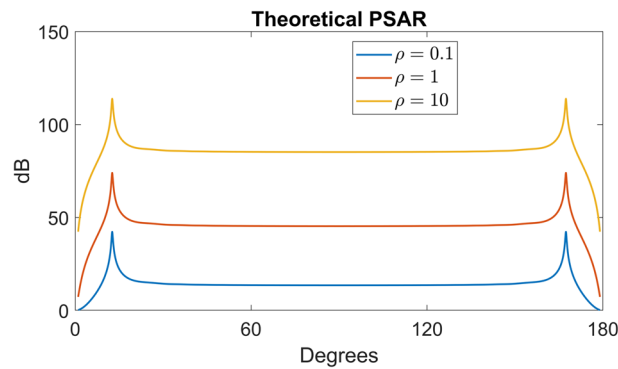


Fig. 6 Theoretical PSAR obtained for a generic triplet line array using different values of the ratio $\rho = \sigma_i/\sigma_n$

zero element to vector \mathbf{g} . In (45), for the matrix $\mathbf{C}^H \mathbf{R}_{z,n}^{-1} \mathbf{C}$ to be invertible, the columns of \mathbf{C} must be independent. This sets an upper limit on how many constraints can be imposed: including the distortionless response constraint, their total number cannot exceed the multiplicity L of the array.

3.6 Choosing parameters σ_n and σ_i

The MVDR beamforming coefficient vector (37) depends on parameters σ_i and σ_n , or, rather, their ratio $\rho = \sigma_i/\sigma_n$. Selection of σ_i and σ_n is guided by the assessment of quality of the resulting beamformer. In [2], the port/starboard ambiguity rejection (PSAR) and array gain were used as theoretical performance indicators for assessment of different beamformers.

To calculate the PSAR parameter [2] for a signal arriving from direction \mathbf{v} , we consider the ratio of the responses of the array steered in the direction of arrival \mathbf{v} and in the ambiguous direction $\hat{\mathbf{v}}$. The mathematical expression has the form

$$\text{PSAR}(\mathbf{v}) = \frac{|\mathbf{h}^H(\mathbf{v})\mathbf{u}_0|^2}{|\mathbf{h}^H(\hat{\mathbf{v}})\mathbf{u}(\hat{\mathbf{v}}, \mathbf{v})|^2}. \tag{50}$$

Figure 6 provides plots of PSAR as a function of the steering angle (measured with respect to the array axis) for different values of ρ . The calculation was carried out for a generic triplet line array. We considered an array made of 32 triplets and assumed that it was non-twisted and its axis was a straight line. The distance between the triplets was 25 cm, which corresponds to an approximate upper design frequency of 3000 Hz. The results in Fig. 6 were obtained for the operating frequency of 2200 Hz.

The plots in Fig. 6 show that the theoretical PSAR increases as the ratio $\rho = \sigma_i/\sigma_n$ increases. We have shown in Sect. 3.4 that when ρ becomes large, the MVDR beamformer (37) turns into the LCMV beamformer (45), for which we have $\mathbf{h}^H(\hat{\mathbf{v}})\mathbf{u}(\hat{\mathbf{v}}, \mathbf{v}) = 0$, so the theoretical PSAR becomes infinite.

Figure 7 shows plots of the array gain AG obtained for the same generic triplet line array using the beamformer (37) under the assumption that the actual noise was isotropic. Noting that

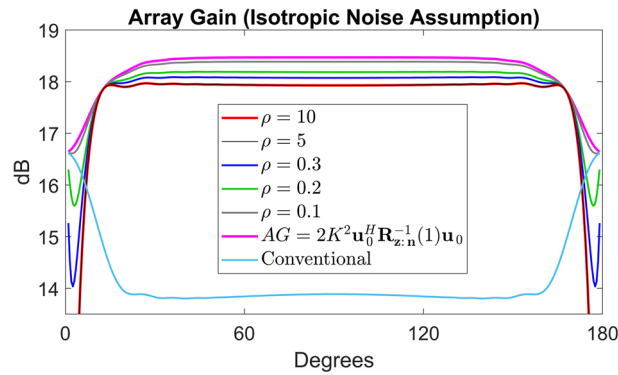


Fig. 7 Theoretical array gain obtained for a generic triplet line array using different values of the ratio $\rho = \sigma_i/\sigma_n$ and comparison with the array gain of the conventional beamformer

$$\begin{aligned} \mathbf{R}_{z:n} &= \mathbf{R}_{z:n}(\sigma_n) = \sigma_n^2 \mathbf{R}_{z:n}(1), \\ \mathbf{R}_{z:ni} &= \mathbf{R}_{z:ni}(\sigma_n, \sigma_i) = \sigma_n^2 \mathbf{R}_{z:ni}(1, \rho), \end{aligned}$$

where the dependence on ν is omitted for brevity, we obtain (cf. 36)

$$AG = AG(\rho) = \frac{2K^2(\mathbf{u}_0^H \mathbf{R}_{z:ni}^{-1}(1, \rho) \mathbf{u}_0)^2}{\mathbf{u}_0^H \mathbf{R}_{z:ni}^{-1}(1, \rho) \mathbf{R}_{z:n}(1) \mathbf{R}_{z:ni}^{-1}(1, \rho) \mathbf{u}_0}. \tag{51}$$

As $\rho \rightarrow 0$, the array covariance $\mathbf{R}_{z:ni}(1, \rho)$ used in the optimal beamformer (37) approaches the array covariance $\mathbf{R}_{z:n}(1)$ associated with the actual noise. As a result, the array gain increases until it reaches the maximal value at $\rho = 0$ where

$$AG = AG_{\max} = 2K^2 \mathbf{u}_0^H \mathbf{R}_{z:n}^{-1}(1) \mathbf{u}_0.$$

For comparison, Fig. 7 provides a plot of the array gain for the conventional beamformer, also obtained under the isotropic noise assumption. In the considered example, when the steering direction is outside of the endfire zones, the array gain of the MVDR beamformer (37) is greater than that of the conventional beamformer by approximately 4 dB.

It is evident from Figs. 6 and 7 that as ρ increases from small to large values, the theoretical PSAR increases, while the theoretical array gain AG decreases. This indicates that selection of σ_n and σ_i used in the MVDR beamforming (37) should be a trade-off between PSAR and AG. However, Fig. 7 shows that the array gain of the MVDR beamformer (37) varies moderately with ρ and, for all values of ρ and steering directions outside of the endfire zones, it exceeds well the array gain of the conventional beamformer. Hence, our focus was elimination of the port/starboard ambiguity.

A compromise value of the synthetic interference-to-noise ratio used in this work was $\rho = 1$. Using the same example of a generic triplet line array, we now demonstrate that the resulting MVDR beamformer (37) achieves high PSAR values by showing that it is nearly the same as the LCMV beamformer (45) across a broad range of frequencies from 1500 Hz to 3000 Hz.

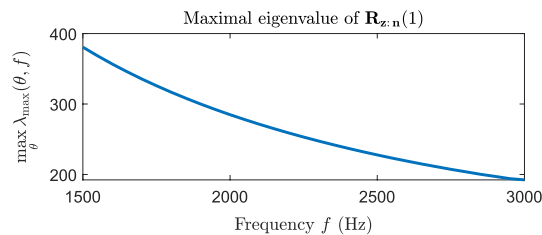


Fig. 8 Plot of $\max_{\theta} \lambda_{\max}(\theta, f)$, where θ is the angle between the horizontal steering direction and the array axis

Consider again the denominator of the fraction in equation (47). If λ_{\max} is the maximal eigenvalue of $\mathbf{R}_{z;n}(1)$, then

$$2\sigma_1^2 K^2 \hat{\mathbf{u}}^H \mathbf{R}_{z;n}^{-1} \hat{\mathbf{u}} \geq 2\rho^2 K^2 \frac{\|\hat{\mathbf{u}}\|^2}{\lambda_{\max}}.$$

For a non-twisted straight line array geometry, we have $\|\hat{\mathbf{u}}\|^2 = L$, which gives

$$2\sigma_1^2 K^2 \hat{\mathbf{u}}^H \mathbf{R}_{z;n}^{-1} \hat{\mathbf{u}} \geq \frac{2\rho^2 K^2 L}{\lambda_{\max}(\mathbf{v}, f)} \geq \frac{2\rho^2 K^2 L}{\max_{\mathbf{v}, f} \lambda_{\max}(\mathbf{v}, f)}. \tag{52}$$

Figure 8 provides a plot of $\max_{\theta} \lambda_{\max}(\theta, f)$, where θ is the angle between the horizontal steering direction and the array axis. Using this plot, we obtain $\max_{\theta, f} \lambda_{\max}(\theta, f) \approx 381$.

Upon substitution of this value, as well as $\rho = 1$, $K = 32$ and $L = 3$ into the right-hand side of (52), we obtain

$$2\sigma_1^2 K^2 \hat{\mathbf{u}}^H \mathbf{R}_{z;n}^{-1} \hat{\mathbf{u}} > 16 \gg 1.$$

Hence, the approximation (48) is valid, and therefore $\mathbf{h}_{\text{MVDR}} \approx \mathbf{h}_{\text{LCMV}}$ for the considered broad band of frequencies.

Similar results can be obtained for noise model (33).

Figure 8 shows a trend that $\max_{\theta} \lambda_{\max}(\theta, f)$ increases as the frequency decreases, so, at some lower frequencies, the condition $2\sigma_1^2 K^2 \hat{\mathbf{u}}^H \mathbf{R}_{z;n}^{-1} \hat{\mathbf{u}} \gg 1$ will not be satisfied, which indicates that the PSAR performance of the considered beamformer will be worse. Generally, both the array gain and the PSAR deteriorate at lower frequencies, so the low-frequency operational limit is defined by the associated performance thresholds.

4 Calculation of PSAR in the broadband case

Equation (50) defines PSAR in the narrowband case. To measure PSAR in the broadband case, we adopt the approach [2–4] based on comparison of processor display intensities at the target and the associated ambiguous locations.

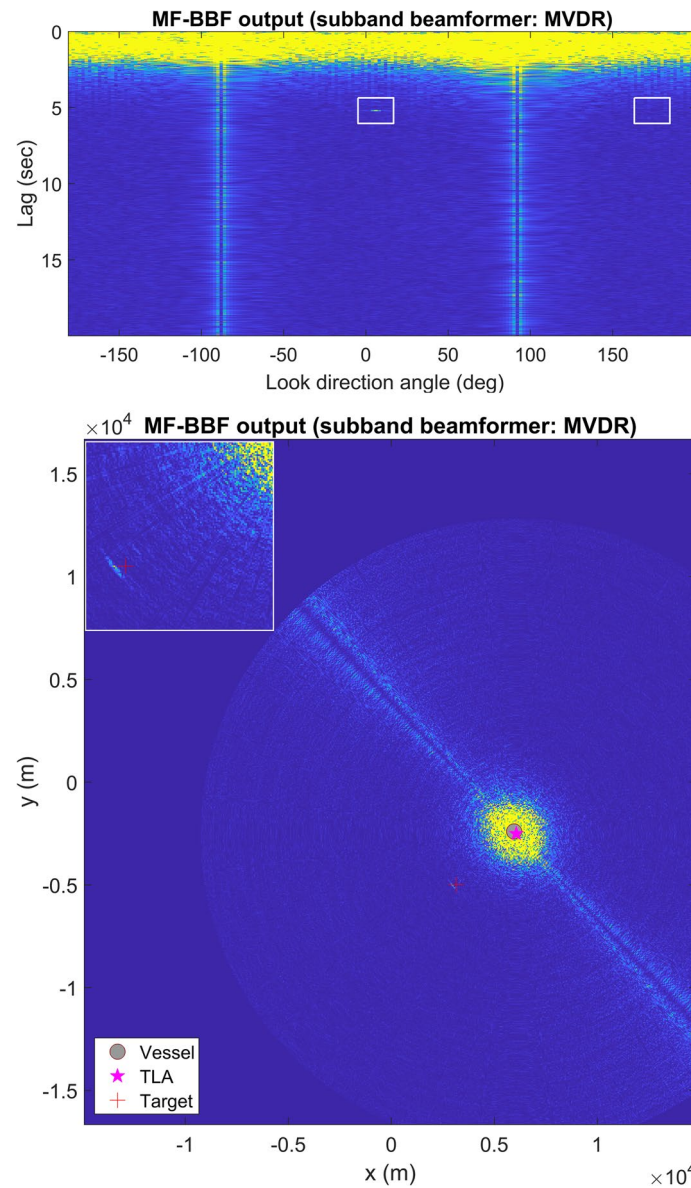


Fig. 9 Processing outputs obtained for SST data; the subband beamformer used: MVDR. The upper left corner of the lower display shows an image obtained by zooming in on the target location

Figure 9 shows output of broadband processing of simulated sonar time series produced using the Sonar Simulation Toolset (SST)¹ [10]. The simulation used inputs (sound velocity profile, bottom depth, source/target/receiver locations/depths, source/receiver array geometries) emulating a snippet of the LCAS'16 trials [3, 4]. The transmission waveform used to generate the simulated sonar time series was a 1 s LFM pulse with a bandwidth of 800 Hz centred at 3100 Hz. LCAS'16 trials employed SLIm

¹ SST was created by a team led by Dr Robert Goddard at the Applied Physics Laboratory, University of Washington (APLUW), Seattle, WA USA. Its development was funded primarily by the US Office of Naval Research (ONR). SST was provided to DSTG through The Technical Cooperation Program (TTCP).

Cardioid Towed Array (SLICTA) receiver. SLICTA is a triplet line array consisting of 64 triplets of hydrophones [4]. The array is also equipped with non-acoustic sensors (NAS) that measure heading, roll and pitch along the array [4]. The processing consisted of broadband beamforming followed by replica cross-correlation. Figure 9 provides a bearing-lag display (where 0 degrees corresponds to the broadside direction) and its mapping onto the Cartesian plane. We used the magnitude of the cross-correlation V as the display intensity. The array shape and receiver element positions used in both the simulation and beamforming were estimated from the corresponding snippet of NAS data using interpolation of the associated rotation matrices and integration. For broadband beamforming, we used 80 equal-width subbands, although, for the considered waveform, using a smaller number of subbands, e.g. 40, gave similar results.

Following the methodology used in [2–4], we define PSAR in the broadband case using the processing output as the ratio

$$\text{PSAR}(\mathbf{r}) = \frac{\max_{D(\mathbf{r})} (|V|^2) - \text{CFAR}_{\mathbf{r}}[|V|^2]}{\max_{D(\hat{\mathbf{r}})} (|V|^2) - \text{CFAR}_{\hat{\mathbf{r}}}[|V|^2]}, \quad (53)$$

where V is the output of the replica cross-correlator, \mathbf{r} and $\hat{\mathbf{r}}$ are the target and the associated ambiguous locations in the bearing-lag plane, and $D(\mathbf{r})$ is a small rectangular domain centred at point \mathbf{r} , while $\text{CFAR}_{\mathbf{r}}[\cdot]$ denotes a 2-dimensional cell-averaging constant false alarm rate (CA-CFAR) [11] smoothing with the test cell at \mathbf{r} . The sizes of the CFAR and the associated gap windows in (53) were chosen using the bearing resolution of the beamformer and the width of the compressed pulse.

For the target highlight in Fig. 9, the resulting PSAR is 19.7 dB. Application of (53) to the outputs obtained using SST echo-only simulation gives a somewhat larger value of PSAR, which indicates that in the presence of the clutter, the employed CFAR averaging underestimates the associated background levels.

Figure 10 shows processing outputs obtained for the snippet of LCAS'16 data emulated in Fig. 9. For the target highlight seen in the provided displays, the obtained PSAR value is 17.9 dB.

Figure 11 provides bearing-lag scans produced for the same snippet of data using the LCMV method and the conventional beamformer. The obtained PSAR values at the considered target location are 17.9 dB and 1.3 dB, respectively.

In comparison with the PSAR values reported in [3] and [4], our MVDR and LCMV PSAR values are somewhat larger. This difference can be explained by the difference in the considered target steering direction, and it can also be attributed to the differences in both the PSAR calculation algorithms and in the used beamforming methods.

5 Conclusions

We have described a broadband beamforming technique that can be employed in processing of data received by multiplet line arrays. Such arrays are increasingly used in undersea surveillance. The considered method is a variant of the subband processor [6]. In this processor, the array signal in each of the subbands is beamformed using a

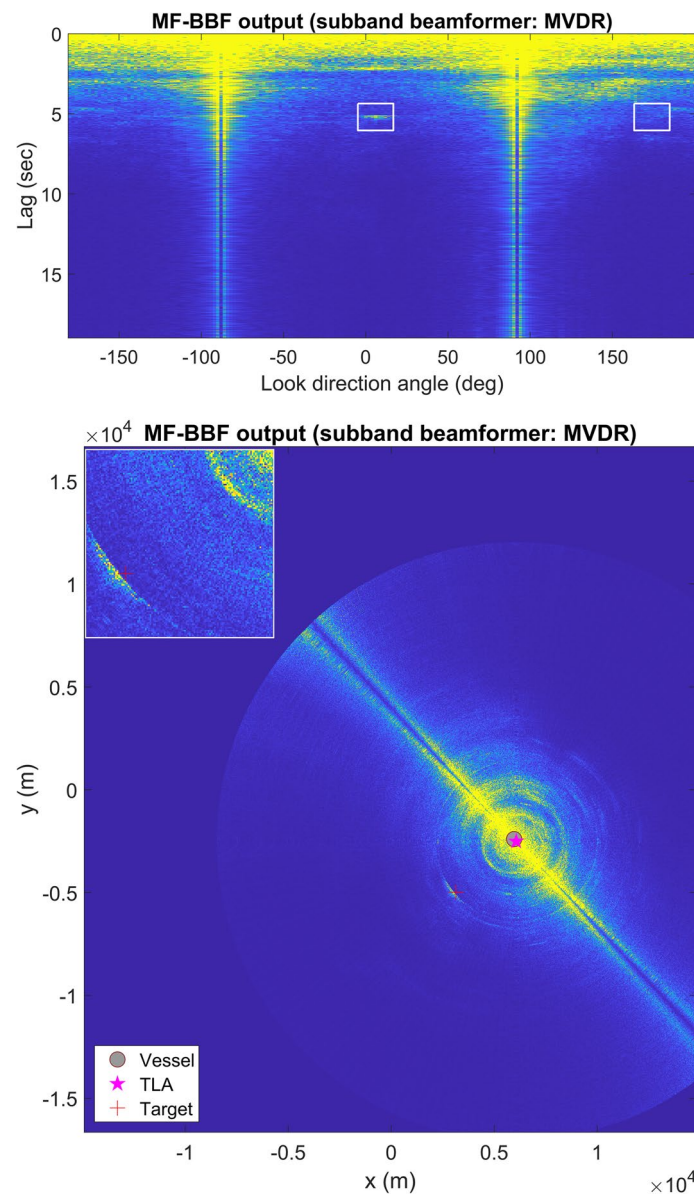


Fig. 10 Processing outputs obtained for LCAS'16 data; the subband beamformer used: MVDR. The upper left corner of the lower display shows an image obtained by zooming in on the target location

narrowband beamformer. Unlike the discrete Fourier transform beamformers [6], which treat each frequency bin as a subband, the considered beamformer operates on subbands made of many frequency bins; as a result, it requires significantly fewer beamforming operations.

The narrowband beamformers used in this work to assemble the broadband beamformer are non-adaptive forms of the beamspace MVDR and LCMV methods designed to eliminate the port/starboard ambiguity. Both techniques produce distortionless response. The beamspace approach used in these methods reduces their computational cost and improves the stability of the covariance matrix inversion. Non-adaptive methods do not require computationally-expensive array covariance estimation and rely only

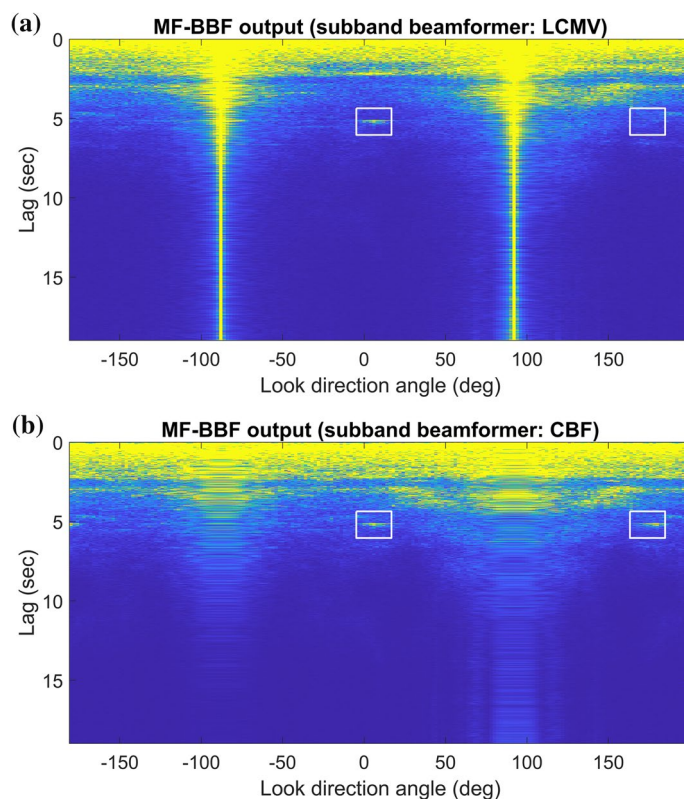


Fig. 11 Processing outputs obtained for LCAS'16 data; the subband beamformer used: **a** LCMV beamformer, **b** conventional beamformer

on the array geometry, which can be estimated using data from non-acoustic sensors. Methods discussed in this paper can handle general multiplet line array geometries.

The considered MVDR scheme is an optimal beamformer that rejects the ambiguity by penalising the artificial interference arriving from the ambiguous direction, while the LCMV method removes the ambiguous contribution by placing a perfect null on the direction of its arrival. The MVDR beamformer depends on the ratio between the powers of the artificially injected interference and the noise. We chose this ratio as a trade-off between the theoretical array gain and the port/starboard ambiguity rejection, and we have also established conditions on this ratio under which the MVDR beamformer turns into the LCMV beamformer. Although both the MVDR and LCMV methods can be used to reject additional interferences with known directions of arrival, the MVDR method can handle such tasks with more flexibility, as, unlike the LCMV method, it is not limited by the upper number of constraints that can be imposed.

The port/starboard ambiguity rejection of the developed broadband beamformer was assessed by comparing the associated display intensities of lag-bearing scans obtained by beamforming and matched filtering of sonar data. We considered both simulated and experimental data. The former were generated using the Sonar Simulation Toolset, while the latter were obtained through the participation in the LCAS trials. The port/starboard ambiguity rejection performance achieved by the MVDR and LCMV

beamformers is similar, showing a considerable improvement compared to the conventional beamformer.

Appendix

Below we provide details of a discrete-time implementation of the broadband beamformer summarised in Sect. 2.

Suppose that the considered multi-channel signal $\mathbf{p}(t)$ is sampled at points $t_n = nT/N$ ($n = 0, \dots, N - 1$), where T is the duration of the listening interval. The discrete Fourier transform and the fast Fourier transform (FFT) algorithm are used to represent the sampled discrete-time signal in the interval $0 \leq t \leq T$ as a continuous function using the finite trigonometric series (FTS)

$$[\mathbf{p}]_q(t) = \sum_{m=-M}^M c_m^q e^{i\frac{2\pi}{T}mt}, \quad (q = 1, \dots, Q), \tag{54}$$

where $M = (N - 1)/2$, if N is odd, and $M = N/2$, if N is even. It is assumed that $2\pi M/T > \omega_{\max}$, i.e. the sampling rate satisfies the Nyquist criterion and so (54) has enough harmonics to represent the entire spectrum of $\mathbf{P}(\omega)$.

Next we represent the beamformed output (10) in terms of the FTS coefficients $\{c_m^q\}$. Define

$$I_s = \{m \mid 2\pi m/T \in \hat{I}_s\}, \quad (s = 1, \dots, N_s). \tag{55}$$

Equation (55) defines sets I_s of indices of frequency bins belonging to respective subbands \hat{I}_s . Although the spectrum of term m in (55) is mostly confined to the associated spectral bin centred at radial frequency $2\pi m/T$, there are also some small contributions from outside of that bin. Assuming that T is sufficiently large, we can ignore such off-bin contributions obtaining

$$[\mathbf{p}_s]_q(t) = \sum_{m \in I_s} \left(c_{-m}^q e^{-i\frac{2\pi}{T}mt} + c_m^q e^{i\frac{2\pi}{T}mt} \right) \tag{56}$$

and

$$[\tilde{\mathbf{p}}_s]_q(t) = 2 \sum_{m \in I_s} c_m^q e^{i\frac{2\pi}{T}mt} e^{-i\omega_s t}. \tag{57}$$

Equation (5) gives

$$[\mathbf{x}_s]_q(t) = 2 \sum_{m \in I_s} c_m^q e^{i\frac{2\pi}{T}m(t-\tau_q)} e^{-i\omega_s(t-\tau_q)}. \tag{58}$$

Note. When Eq. (56) is considered outside the interval $0 \leq t \leq T$, its right-hand side has to be multiplied by a rectangular window function $H_T(t)$, such that $H_T(t) = 1$, if $0 \leq t \leq T$, and $H_T(t) = 0$, otherwise. In Eq. (58), we do not take into account the edge effects associated with the resulting factors $H_T(t - \tau_q)$. Such edge effects can be ignored if $[\mathbf{p}_s]_q(t_n)$ becomes negligibly small in the intervals $0 \leq t \leq \max_q(|\tau_q|)$ and

$T - \max_q(|\tau_q|) \leq t \leq T$. If the bandwidths of \hat{I}_s are not too small, this can be achieved by isolating each record $[\mathbf{p}]_q(t_n)$ from the edges $t = 0$ and $t = T$ using an appropriate windowing function. This would naturally imply that the considered signal must be confined within the associated window.

Substitute (58) into (10) to obtain

$$y(t) = 2 \sum_{s=1}^{N_s} \sum_{q=1}^Q w_q^*(\omega_s) \sum_{m \in I_s} c_m^q e^{i\frac{2\pi}{T} m(t-\tau_q)} e^{-i\omega_s(t-\tau_q)} e^{i(\omega_s-\omega_0)t}.$$

This can be transformed to

$$y(t) = \sum_{q=1}^Q \gamma_q(t), \tag{59}$$

where

$$\gamma_q(t) = 2 \sum_{s=1}^{N_s} \sum_{q=1}^Q w_q^*(\omega_s) \sum_{m \in I_s} c_m^q e^{i\frac{2\pi}{T} m(t-\tau_q)} e^{-i\omega_s(t-\tau_q)} e^{i(\omega_s-\omega_0)t}. \tag{60}$$

and

$$\gamma_m^q = \begin{cases} w_q^*(\omega_s) c_m^q e^{i(\omega_s - \frac{2\pi}{T} m)\tau_q}, & \text{if } m \in I_s, \text{ and} \\ & s = 1, \dots, N_s \\ 0, & \text{otherwise.} \end{cases} \tag{61}$$

Introducing

$$\gamma_m = \sum_{q=1}^Q \gamma_m^q, \tag{62}$$

we can rewrite (59) as

$$y(t) = 2 \sum_{m=0}^M \gamma_m e^{i\frac{2\pi}{T} mt} e^{-i\omega_0 t} \tag{63}$$

Considering $y(t)$ at $t = t_n = nT/N$ ($n = 0, \dots, N - 1$), we obtain

$$y(t_n) = 2 \sum_{m=0}^M \gamma_m e^{in\frac{2\pi}{N} m} e^{-i\omega_0 t_n},$$

or, since $\gamma_m = 0$, when $m > M$,

$$y(t_n) = 2 \left[\sum_{m=0}^{N-1} \gamma_m e^{in\frac{2\pi}{N} m} \right] e^{-i\omega_0 t_n} \tag{64}$$

The expression in the square brackets in (64) can be readily calculated using the inverse FFT.

Equations (61), (62) and (64) constitute a discrete-time implementation of a broadband subband beamformer (10).

Similarly to Sect. 2, in order to show that the resulting broadband beamformer does not distort the signal, consider a signal arriving from some fixed look direction \mathbf{v} . Suppose that the associated contribution to the dynamic pressure at the centre of the array is a band-limited function that can be represented using FTS as follows

$$g(t) = \sum_{m=-M}^M b_m e^{i\frac{2\pi}{T} mt} = \sum_{m=0}^M \left(b_m^* e^{-i\frac{2\pi}{T} mt} + b_m e^{i\frac{2\pi}{T} mt} \right). \tag{65}$$

It is assumed in (65) that $b_m = 0$ if $m \notin \bigcup_{s=1}^{N_s} I_s$. The resulting complex envelope of the signal component in subband s at receiver q is

$$\begin{aligned} [\tilde{\mathbf{p}}_s]_q(t) &= \tilde{g}_s(t + \tau_q) e^{i\omega_s \tau_q} \\ &= 2 \sum_{m \in I_s} b_m e^{i\frac{2\pi}{T} m(t+\tau_q)} e^{-i\omega_s(t+\tau_q)} e^{i\omega_s \tau_q} \\ &= 2 \sum_{m \in I_s} b_m e^{i\frac{2\pi}{T} m\tau_q} e^{i\frac{2\pi}{T} mt} e^{-i\omega_s t}, \end{aligned} \tag{66}$$

where τ_q is given by (6). To utilise (61), note that in the considered case,

$$c_m^q = b_m e^{i\frac{2\pi}{T} m\tau_q}$$

(see Eq. (57)). Hence,

$$\gamma_m^q = \begin{cases} w_q^*(\omega_s) b_m e^{i\omega_s \tau_q}, & \text{if } m \in I_s, \text{ and} \\ & s = 1, \dots, N_s \\ 0, & \text{otherwise.} \end{cases} \tag{67}$$

If each beamforming vector $\mathbf{w}(\omega_s)$ satisfies the distortionless response condition (8), then

$$\gamma_m = \sum_{q=1}^Q \gamma_m^q = b_m \sum_{q=1}^Q w_q^*(\omega_s) e^{i\omega_s \tau_q} = b_m \mathbf{w}^H(\omega_s) \mathbf{v}_s(\mathbf{v}) = b_m.$$

Therefore,

$$y(t) = 2 \sum_{m=0}^M \gamma_m e^{i\frac{2\pi}{T} mt} e^{-i\omega_0 t} = 2 \sum_{m=0}^M b_m e^{i\frac{2\pi}{T} mt} e^{-i\omega_0 t} = \mathcal{C}_{\omega_0}[g(t)]. \tag{68}$$

Equation (68) shows that similarly to (13), the discrete-time implementation of the broadband beamformer (10) does not change the signal component of the array input.

Abbreviations

- MVDR Minimum Variance Distortionless Response
- MPDR Minimum Power Distortionless Response
- LCMV Linear Constraint Minimum Variance
- LCMP Linear Constraint Minimum Power
- LCAS Littoral Continuous Active Sonar
- NAS Non-Acoustic Sensor
- FFT Fast Fourier Transform

MATLAB	MATrix LABoratory
PSAR	Port/starboard ambiguity Rejection
CA-CFAR	Cell-Averaging Constant False Alarm Rate
SLICTA	SLIm Cardioid Towed Array
TLA	Towed Line Array
SST	Sonar Simulation Toolset

Acknowledgements

The use of LCAS data was made possible by LCAS multi-National Joint Research Project (MN-JRP) with participation from the NATO Centre for Maritime Research and Experimentation, Defence Science and Technology Group (AUS), Department of National Defence Research and Development Canada (CAN), Defence Science and Technology Laboratory (GBR), Centro di Supporto e Sperimentazione Navale-Italian Navy (ITA), Norwegian Defence Research Establishment (NOR), Defence Technology Agency (NZL) and the Office of Naval Research (USA).

Author contributions

The first author has developed and evolved the algorithm. The second author suggested improvements and provided assistance with data handling. Both authors read and approved the final manuscript.

Declarations

Competing interests

The authors declare that they have no competing interests.

Received: 6 November 2022 Accepted: 18 January 2023

Published online: 16 February 2023

References

1. D.T. Hughes, Aspects of cardioid processing. SACLANTCEN report SR-329, SACLANT Undersea Research Centre, La Spezia, Italy (2000)
2. J. Groen, S.P. Beerens, R. Been, Y. Doisy, E. Noutary, Adaptive port-starboard beamforming of triplet sonar arrays. *IEEE J. Ocean. Eng.* **30**(2), 348–359 (2005). <https://doi.org/10.1109/JOE.2005.850880>
3. P. Stinco, A. Tesei, A. Maguer, F. Ferraioli, V. Latini, L. Pesa, Sub-bands beam-space adaptive beamformer for port-starboard rejection in triplet sonar arrays, in *2018 IEEE Global Conference on Signal and Information Processing (GlobalSIP)* (2018), pp. 236–240. <https://doi.org/10.1109/GlobalSIP.2018.8645970>
4. G. Canepa, A. Tesei, L. Troiano, S. Biagini, F. Aglietti, R. Dymond, M. Mazzi, A. Vermeij, V. Grandi, Comparison of computation time and accuracy of the real time implementation of two beamforming algorithms, in *Underwater Acoustics Conference and Exhibition 2017 (UACE 2017)* (2017), pp. 121–128
5. S. Simakov, Z.Y. Zhang, R.P. Goddard, Optimal beamforming on synthetic interference and noise for active processing of multiplet line arrays, in *2015 IEEE International Conference on Acoustics, Speech and Signal Processing (ICASSP)* (2015), pp. 2519–2523. <https://doi.org/10.1109/ICASSP.2015.7178425>
6. H.L. Van Trees, *Optimum Array Processing, Part IV of Detection, Estimation, and Modulation Theory. Detection, Estimation, and Modulation Theory* (John Wiley and Sons Inc., New York, 2002)
7. D.A. Gray, Formulation of the maximum signal-to-noise ratio array processor in beam space. *J. Acoust. Soc. Am.* **72**(4), 1195–1201 (1982). <https://doi.org/10.1121/1.388328>
8. R.N. McDonough, A.D. Whalen, *Detection of Signals in Noise* (Academic Press, San Diego, 1995)
9. W.S. Burdic, *Underwater Acoustic System Analysis* (Prentice-Hall, Hoboken, NJ, 1984)
10. R.P. Goddard, The sonar simulation toolset, release 4.6: Science, mathematics, and algorithms. Technical Report APL-UW TR 0702, Applied Physics Laboratory, University of Washington, Seattle, WA (2000)
11. M.A. Richards, J.A. Scheer, W.A. Holm, *Principles of Modern Radar: Basic Principles*, vol. 1 (Institution of Engineering and Technology, Italy, Genoa, 2010)

Publisher's Note

Springer Nature remains neutral with regard to jurisdictional claims in published maps and institutional affiliations.